Title

A Comparison of the Detection Sensitivity of the Poisson Clutter Split and Region of Interest Algorithms on the RadMAP Mobile System

Journal

IEEE Transactions on Nuclear Science, 63(2)

ISSN

0018-9499

Authors

Joshi, TH
Cooper, RJ
Curtis, J
et al.

Publication Date

2016-04-01

DOI

10.1109/tns.2016.2537206

Peer reviewed

A Comparison of the Detection Sensitivity of the Poisson Clutter Split and Region of Interest Algorithms on the RadMAP Mobile System

T.H. Joshi, R.J. Cooper, J. Curtis, M. Bandstra, B.R. Cosofret, K. Shokhirev, and D. Konno

***Abstract*—This analysis uses source injection into background data collected by the Radiological Multi-sensor Analysis Platform (RadMAP) to characterize the performance of the Poisson Clutter Split algorithm and compare it with a region-of-interest algorithm. This comparison is performed for varying detector array sizes and false alarm rates using data from Sodium Iodide and High Purity Germanium detector arrays. The application of the Poisson Clutter Split algorithm is found to yield significant performance gains for both medium- and high-resolution detector arrays. Furthermore, trade offs between energy resolution, array size, cost, and detection performance are explored. In doing so, it is shown that the choice of detection algorithm is a key factor in determining the overall system performance and should be an important consideration in system design.**

***Index Terms*—Gamma-ray detection, Radioactive source search, Gamma-ray spectral analysis, Homeland security**

I. Introduction

THE standoff detection of γ-ray sources (radiological and special nuclear material) is challenging due to the large natural variations of γ-ray background in the environment [1]–[4]. To improve detection sensitivity, one may consider increasing the size of a detector array as a means of increasing event-rate, employing higher resolution detectors to increase the specificity of detected events, or developing advanced algorithms that enable improved background estimation.

Previous work has explored the trade-offs between detector resolution, detector array size, and imaging in the context of region-of-interest type (RoI) detection algorithms, [2]–[4]. One approach to reducing the impact of natural variations in γ-ray backgrounds is the deployment of coded aperture imagers [3]. Recent work, however, using the passively coded NaI array in RadMAP to search for unshielded sources, with a coded mask that optimizes the point spread function in the fully coded field of view, has demonstrated that despite the ability to reduce background in image pixels, passively coded arrays are not able to reach the detection sensitivity of an un-masked array employing spectral detection techniques [4]. The inability of traditional detection algorithms, using integrated count rates or count rates within a region of interest (RoI), to effectively account for natural radiological backgrounds and their variation has led to the development of more advanced algorithms that are capable of accurate estimation of the background using information from the entire spectrum. Many approaches to improve detection and/or identification have been demonstrated. Examples of such approaches include: the utilization of ratios of counts within spectral windows to suppress background variability [5], application of principal components analysis and maximum likelihood estimation [6], [7], algorithms that seek to match pre-computed spectral templates [8], [9], and attempts to use neural networks [10]. For further discussion about detection and identification approaches that have been applied to γ-ray spectra we refer the reader to [1], [7], [11] and references therein.

The performance of PCS has previously been described using check sources and several detectors in various configurations [12]. In this article, using source injection and a dataset from the Radiological Multi-sensor Analysis Platform (RadMAP) [4], [13], the performance of PCS is characterized for both medium- and high- resolution detector arrays of varying sizes, and compared with a RoI algorithm that uses trained background estimation. This work uses the very large dataset collected by RadMAP, across a variety of urban, suburban, and rural environments, to explore the performance of two algorithms with background variability and false alarm rates (FAR) representative of those expected in mobile urban search scenarios. The presented results enable comparisons between the performance of PCS and an RoI algorithm.

The RadMAP vehicle is based on the Mobile Imaging and Spectroscopic Threat Identification (MISTI) vehicle built by the Naval Research Laboratory for the Domestic Nuclear Detection Office's Standoff Radiation Detection System (SORDS) program [14]. The RadMAP truck carries a 10×10 array of $10\times10\times5\,\mathrm{cm}^3$ NaI detectors behind a coded mask and 24 100% relative efficiency HPGe detectors (Fig. 1 inset). The simultaneous collection of high- and medium-resolution γ-ray data with large detector arrays, in addition to a variety of additional sensors, makes RadMAP a unique tool for measuring and studying the variations in natural radiological backgrounds over large areas, and investigating correlations with data from contextual sensors. The dataset used in this analysis was acquired over a three month period around the San Francisco Bay Area. Across the three months of acquisition, data collection was performed on 22 days and spanned urban, suburban, and rural environments (Fig. 1). A

Manuscript received October 22, 2015; revised January 21, 2016; accepted February 23, 2016. The project was funded by the US Department of Homeland Security, Domestic Nuclear Detection Office (DNDO) under contract number HSQDC-13-X-B0003. This support does not constitute an express or implied endorsement on the part of the Government.

T.H. Joshi, R.J. Cooper, J. Curtis, and M. Bandstra are with Lawrence Berkeley National Laboratory, Berkeley, CA 94720 USA (email:thjoshi@lbl.gov).

B.R. Cosofret, K. Shokhirev, and D. Konno are with Physical Sciences Inc., Andover, MA 01810 USA.

Digital Object Identified 10.1109/TNS.2016.2537206

Fig. 1. (Color online) Map of the San Francisco Bay Area with locations of data collection shown in white. Inset: Image of RadMAP with overlaid CAD drawing showing the NaI and HPGe detector arrays.

subset of this data, where the truck was traveling on a straight path for $>$ 200 m, was selected for analysis, yielding 14.1 hours of data for the estimation of background variability and 1.0 hour of data used for testing the algorithms using source injection. This article presents a study of the performance of PCS, relative to RoI, on detection sensitivity for both medium (NaI) and high (HPGe) resolution detector arrays of varying size.

II. Methods

A. Data Collection and Segmentation

The data used in this study is a subset of that collected by RadMAP from March to May of 2012. During the period of data collection there were 99 functioning NaI detectors and a minimum of 14 functioning HPGe detectors. Calibration measurements were performed daily before data acquisition. Gain stabilization was performed prior to analysis using K40 and Tl208 peaks. At 1460 keV, individual NaI detector resolution spanned 6-11% FWHM and the composite energy resolution of the entire NaI array was 7% FWHM.

During data collection a $\sim$50% opacity passive coded mask was present in front of the NaI detector array. While the presence of this passive mask is not ideal for the study of spectroscopic detection, which is the focus of this article, acquisition with the mask in place is the default configuration of RadMAP. While the focus of this study is on spectroscopic detection this dataset was previously used to explore trade-offs in imaging and spectroscopy [4]. Data from this configuration was utilized for study because it gave access to the large amount of data collected by RadMAP, which in turn allowed the study of spectroscopic detection algorithms at low false alarm rates (FAR). The presence of the coded mask systematically decreases the photopeak efficiency of the array by $\sim 50\%$ at 662 keV while only diminishing background rates by $\sim 10-25\%$ [13]. To remind the reader of the presence of a 50% opaque coded mask in front of the NaI array, we refer to the number of NaI detectors being considered in our analysis as ν^*, where ν is the number of detectors being effectively sampled and the asterisk implies presence of the coded mask. The majority of results presented in Section III are left in terms of size of a masked NaI array, however for comparisons of size and cost against performance we estimate the equivalent number of unmasked NaI detectors. Discussion of this estimate is presented in Appendix A.

The RadMAP data used in this study is consistent with that used in [4], where we only analyze *segments* where the truck was traveling in a straight line for $>$ 200 m. Traveling in a straight line is defined as deviation of more than 5 m, over the 200 m span, from a linear best fit to the INS data points. Segments where the truck speed remained 15 ± 3 mph (6.7 ± 1.3 m/s) were selected as the testing (I) subset and used for source injection. The remainder of the segments (E) were used for algorithm-driven background estimation. This approach produced 174 and 1481 segments in testing and background estimation sets, respectively, $I = \{I_1 \dots I_{174}\}$ and $E = \{E_1 \dots E_{1481}\}$, corresponding to 1.0 and 14.1 hours of data. Listmode data from each segment, $D \in \{I, E\}$, was used to produce a series of spectra, $D_n = \{H_{Dn}(i_0) \dots H_{Dn}(i_t)\}$, where $H_{Dn}(i_x)$ refers to the x^{th} spectrum of segment H_n, an integration time of two seconds is used, and all detectors are summed over. An integration time (t_{int}) of two seconds was selected as being consistent with the implementation of PCS for mobile systems. An optimal value for RoI integration may be calculated for constant background environments, the RadMAP dataset, however, is interesting because it samples a variety of environments where the background does vary over short spatial/temporal ranges. The two-second integration time used in this study is not optimized, but the method for optimizing this type of analysis in complex environments is a topic of active research. Bin widths of one and three keV were used for the HPGe and NaI detector arrays, respectively.

A binomial down-sampling of the spectra was utilized to synthesize datasets representative of smaller detector arrays. The probability of acceptance for binomial down-sampling was taken as the fraction of the original array that was desired. This method was selected, rather than simple exclusion of randomly selected detectors, so as to avoid the confounding factor of differences in detector location on the variation of measured background. The number ν and type τ of detectors represented in each segment or spectra are designated with the notation ${}^{\nu}_{\tau}D$. Fig. 2(a,b) shows segment ${}^{99^*}_{N}I_{85}$, a segment of data from the complete NaI detector array. The segment is shown as a two-dimensional histogram of γ-events as a function of time and energy with logarithmic color scaling.

B. Source Injection

Two different isotopes, ^{137}Cs and ^{133}Ba, were used for source-injection in this study. These isotopes are conventional calibration isotopes, span a relevant portion of the spectrum for

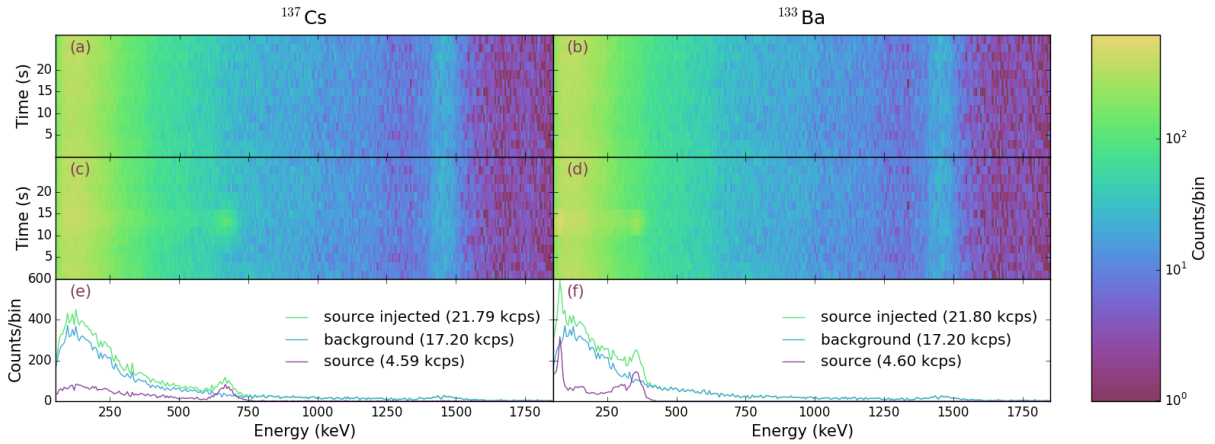

Fig. 2. (Color online) Illustration of source injection using segment ${}^{99^*}_{N}I_{85}$. The distance from the source at closest approach is 20 m. In subplots a and b the segment is shown as a two-dimensional histogram of γ-events as a function of time and energy with logarithmic color scaling. Subplot c(d) shows the same segment following injection of counts from a 400 μCi ^{137}Cs (^{133}Ba) source, ${}^{99^*}_{N}I_{85}(^{137}\mathrm{Cs}, 400\,\mu\mathrm{Ci})$ and ${}^{99^*}_{N}I_{85}(^{133}\mathrm{Ba}, 400\,\mu\mathrm{Ci})$ centered at $t = 13$ s. Subplot e(f) shows the background, source, and source-injected γ-ray spectra, and integral count rates in kilo-counts per second (kcps), at closest approach to the source, $t = 13$ s, for ^{137}Cs (^{133}Ba).

mobile threat detection, and give an example of isotopes with one (^{137}Cs) and several (^{133}Ba) characteristic γ rays. Source only data for injection was produced using two methods: experimental acquisition (^{137}Cs) and simulation (^{133}Ba), the acquisition and processing of the source data is described in detail in the later half of this section.

Source injection analysis was performed using the testing data subset, I, which contains background data collected when the vehicle was traveling at 15 ± 3 mph. Injections were performed assuming 20 m closest approach, a constant velocity of 15 mph, and unshielded sources held 1 m above the ground. Source data, $H_S(X, A, i)$, from a source of isotope X, activity A and corresponding to the position of RadMAP at time i, is injected into a background spectrum, $H_{In}(i)$, producing an injected spectrum,

$$H_{In}(X, A, i) = H_{In}(i) + H_S(X, A, i). \quad (1)$$

The time-dependence of the source data is defined such that the closest approach to the source occurs at the center segment. A source injected segment is then defined as,

$$I_n(X, A) = \{H_{In}(X, A, i_0) \ldots H_{In}(X, A, i_t)\}. \quad (2)$$

Source activities ranging from 5 to 600 μCi in increments of 5 μCi were used for injection studies. Figure 2 illustrates injection of a 400 μCi ^{137}Cs source (left) and a 400 μCi ^{133}Ba source (right) in to ${}^{99^*}_{N}I_{85}$, the 85th segment in the testing set as measured by 99^* NaI detectors. The spectra, before and after source injection, at closest approach to the source is shown in Fig. 2(e,f).

Experimental source data was acquired with a 4 mCi ^{137}Cs source at a controlled outdoor facility. A systematic uncertainty of 5% on the source activity is included for ^{137}Cs results. The source was positioned in a field, 20 ± 1 m from the RadMAP detector array at closest approach, and data was acquired with RadMAP while driving past the source along a straight 100 m section of road at 15 mph. The uncertainty in distance of closest approach during the experiment results in an additional 10% systematic uncertainty for the ^{137}Cs data. This was repeated ten times. A background data set was also acquired on the same roadway by measuring for 27 minutes with RadMAP stationary at the position of closest approach to where the source has been. Data from each lap of the truck past the source was binned into two second spectra and the source term then calculated by subtracting the time-normalized histogram of background data from each two second spectra of source data. The background-subtracted spectra from each lap past the source, $H_S(^{137}\mathrm{Cs}, 4\,\mathrm{mCi}, i)$, were then used for injection into the background segments of the testing dataset. Probabilistic binomial down-sampling was used to synthesize source-injection data representative of weaker sources.

In the case of ^{133}Ba, no experimental data was available. Instead, a simulation using v4.0 of SWORD [15], a monte-carlo simulation toolset, with a GEANT4 back end, was used to produce a series of source spectra for injection. This simulation included a detailed geometry of the RadMAP truck and the detector arrays and included both ground and air-scatter [16]. The simulation was performed for a 101.4 mCi source at positions corresponding to $0, \pm1, \pm2, \pm3$ seconds from closest approach at a speed of 15 mph (6.7 m/s). Results from the simulations were then combined to yield a set of two-second spectra which form $H_S(^{133}\mathrm{Ba}, 101.4\,\mathrm{mCi}, i)$. The simulation was repeated for ^{137}Cs and used for validation of the simulations with experimental data. The simulation was found to be in agreement to within 10% for both photo-peak amplitude and peak/total ratio and a 10% systematic uncertainty is included for ^{133}Ba results. Agreement between simulation and experiment was also found in the case of datasets collected with an un-masked array NaI array [16], adding further confidence that the quality of the simulations were sufficient for use in this study.

C. The RoI Algorithm and its Statistical Limit

Using the background estimation and testing sets, E and $I(X, A)$, two algorithms for detection and identification of

TABLE I
REGION OF INTEREST ENERGY WINDOWS (KEV)

Isotope	Detector	P	B_1	B_2
^{137}Cs	HPGe	659–665	665–674	650–659
	NaI	632–692	692–752	752–812
^{133}Ba	HPGe	354–358	358–364	348–354
	NaI	336–376	400–420	420–440

threat sources were studied: trained region-of-interest (RoI) and Poisson Clutter Split (PCS). The trained RoI algorithm, also used in [4], defines an energy window around the photo-peak of interest that contains source, S, and background, B, contributions, and the sum of all events in this window is $P = S + B$. An estimate of the contribution of background within this window (B_e) is calculated using the sum of measured events within two nearby energy windows ($B_{1,2}$) such that $B_e = a_0 + a_1 B_1 + a_2 B_2$. The energy windows used in the RoI analysis are listed in Table I. The factors, a_i, are calculated from a least squares fit to the segments in the background estimation set, E. The source contribution in a given spectrum is then estimated to be $S_e = P - B_e$. A detection threshold, T_{RoI}, may then be set based on a specified FAR using the 14.1 hours of background estimation data. This trained RoI approach differs from the background-estimating RoI approach in [14] in that the weighting of background estimation windows is not equal and is calculated with training data, and that the threshold for detection is based on measured data rather than the cumulative distribution function of the Poisson distribution.

The statistical limit for detection of RoI is defined as the sensitivity that may be achieved in the situation where the mean background contribution within the photo-peak window ($\overline{B}$) is known for each spectrum and measurement of it is subject only to Poisson fluctuation. In this situation, the detection threshold T_{SL} for each spectrum, such that when $S + B - \overline{B} > T_{SL}$ an alarm is signaled, is calculated as $T_{SL} = k - \overline{B}$ where k is the smallest integer that satisfies $Q(k, \overline{B}) > (1 - t_{int} * \text{FAR})$, where Q is the regularized gamma function, which represents the cumulative distribution function of the Poisson distribution. Our implementation of source injection allows knowledge of the true value of the background (B) and source (S) in each spectrum. Using this information, we calculate the statistical limit for detection of RoI under the assumption that the measured background approximates the mean background $\overline{B} = B$. The probability that a spectrum (H) does *not* produce an alarm, $P_{na}(H) = Q(k+1, \overline{B})$ where $k = T_{SL} - S + \overline{B}$ is then calculated. The value k is increased by one in this calculation because we define an alarm as a situation where the threshold is exceeded. The probability that one or more of the spectra of a segment *does* result in an alarm, in the statistical limit of RoI, P_a, is calculated with as:

$$P_a\big(I_n(X,A)\big) = 1 - \prod_{i=0}^{t} P_{na}\big(H_{In}(X,A,i)\big) \qquad (3)$$

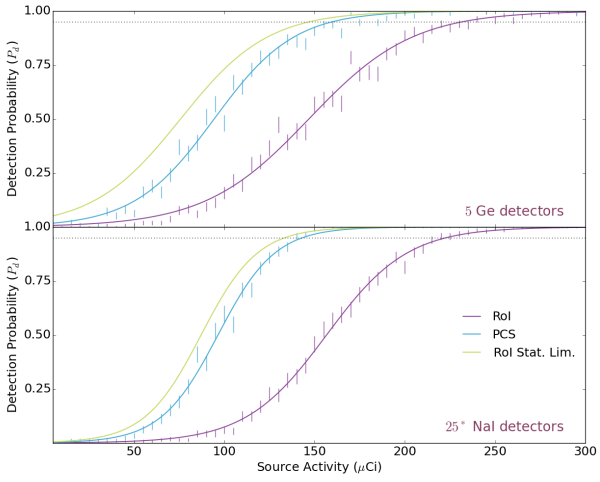

Fig. 3. (Color online) Calculated detection probability as a function of source activity for a ^{137}Cs source and 5 HPGe (top) and 25* NaI (bottom) detectors at $1/7\,\text{hr}^{-1}$ FAR. Dotted horizontal lines indicate 95% P_d. PCS significantly out performs the RoI detection algorithm in both medium- and high-resolution detectors, and approaches the statistical limit of RoI in both cases. Statistical binomial errors are shown, a systematic uncertainty on ^{137}Cs source activity of 5% is not shown.

D. The Poisson-Clutter Split (PCS) Algorithm

The Poisson-Clutter Split (PCS) algorithm was developed to accurately mitigate the two sources of randomness in the radiological spectra, background clutter, i.e. changes in the energy-dependent count rate due to variations in isotopic composition at different locales, weather conditions, etc..., and the random nature of radioactive decay. PCS uses a novel probabilistic representation of radiological backgrounds, accurate modeling of γ-counts based on Poisson statistics, and a Generalized Likelihood Ratio Test to simultaneously perform detection and identification. A model of background clutter, at the core of PCS, was generated based on the analysis of a representative set of spectra collected across multiple environments (a subset of dataset E). From this background set, the PCS algorithm calculates the mean rate as a function of energy as well as the dominant and non-linear modes of spectral variation. The PCS background clutter model allows estimation of the expected mean rate of any new spectrum and the probability of encountering such a rate within the environment. The resulting background estimation (model) is then used to assess the presence of a threat signature in a given spectrum, while at the same time performing isotope identification via full spectral correlation against a known set of isotope library spectra [12].

Through the use of this background model to estimate the magnitude and variability of natural radiological backgrounds, PCS is able to maintain high values of detection probability at very low false alarm rates. A random subset of 6,000 spectra from the background set, E, were used to produce a PCS background model, while the remaining spectra in E were used to determine isotope specific thresholds for FAR of $1/2\,\text{hr}^{-1}$ and $1/7\,\text{hr}^{-1}$. Using the same background model,

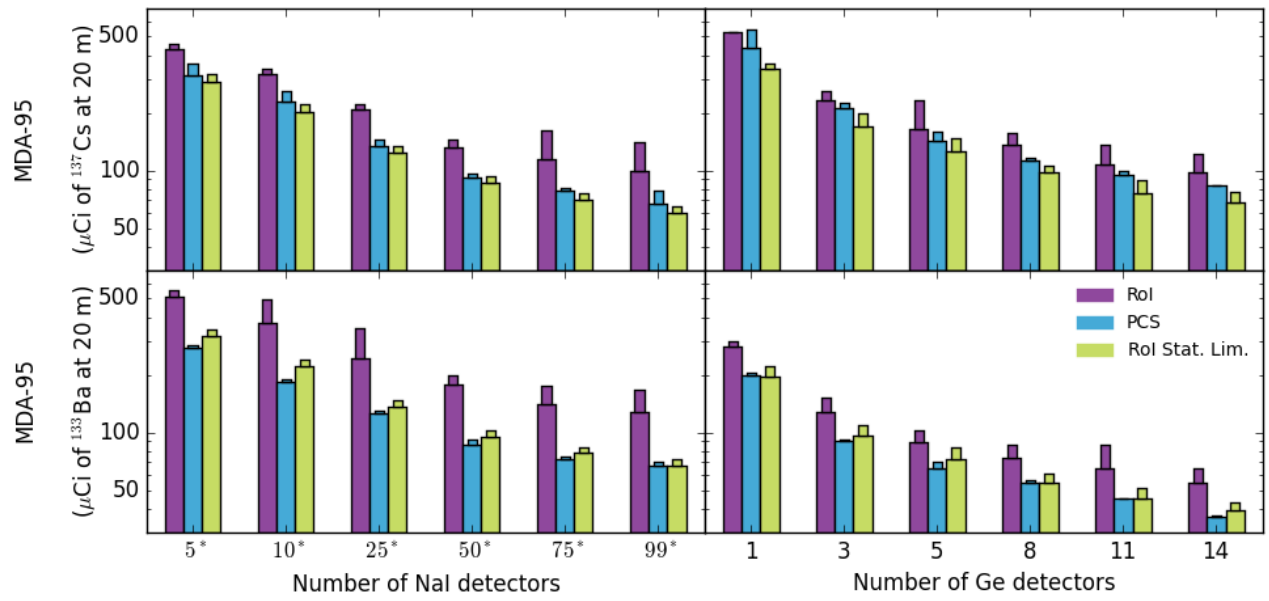

Fig. 4. (Color online) Upper (lower) plots show MDA_{95}, in log-scale, for ^{137}Cs (^{133}Ba) sources at 20m closest approach for each detector array size studied. MDA_{95} are shown for FAR of $1/2\,\mathrm{hr}^{-1}$ ($1/7\,\mathrm{hr}^{-1}$) with wide (narrow) bars. Systematic and statistical uncertainties are not shown for clarity but are listed in Tables II & III.

spectra in the injection set, I, were analyzed to determine whether a given spectrum yields a PCS response above the pre-defined FAR threshold.

E. Calculating detection probability

The same set of source-injected spectra, with injections for source activities ranging from 0 to 600 μCi in steps of 5 μCi for ^{137}Cs and ^{133}Ba, were processed using both algorithms. For each spectrum, the response of an algorithm was compared against the corresponding thresholds, to determine whether an alarm occurred. If an algorithm registered one or more alarms within a segment, the algorithm is considered to have successfully detected the injected source in that segment.

As a means of comparing algorithm performance, the probability of detection (P_d) for a particular scenario (τ, ν, X, A, FAR, algorithm) is defined to be the fraction of the testing segments where an alarm was successfully produced for the correct isotope. In the case of the statistical limit of RoI, P_d is defined as the average of P_a over all injected segments. The Jeffreys interval [17] was used to calculate 68% confidence limits for the calculated values of P_d based on the statistical sample of segments.

III. Results

To examine how the detection sensitivity of RoI and PCS varies with detector array size and detector type, background estimation and source injection sets, T and I respectively, were produced corresponding to $\nu \in \{1, 3, 5, 8, 11, 14\}$ for $\tau =$ HPGe and $\nu \in \{5, 10, 25, 50, 75, 99\}^*$ for $\tau =$ NaI. The testing datasets were produced for source activities ranging from 5 to 600 μCi in increments of 5 μCi for both ^{137}Cs and ^{133}Ba.

P_d was then evaluated across the available parameter space for FAR of $1/2\,\mathrm{hr}^{-1}$ and $1/7\,\mathrm{hr}^{-1}$, allowing exploration of P_d as a function of (X, A, τ, ν, FAR, algorithm). The performance of algorithms in the space of P_d vs. A for fixed FAR, τ, ν, and X may then be visualized, as in Fig. 3. In analyzing P_d vs. A a sigmoid of form $(1+\exp[-k(A-A_0)+c])^{-1}$ was fit to the data to both aid in visualizing the data and also calculating the minimum detectable activity (MDA). MDA_{95} is defined as the activity where the sigmoid fit to P_d reaches 95%.

The example shown in Fig. 3 illustrates P_d as a function of source activity for the detection of a ^{137}Cs source in the cases of (ν, τ) of (5, Ge) and (25^*, NaI) at a $1/7\,\mathrm{hr}^{-1}$ FAR. For both high- and medium-resolution arrays PCS approaches the statistical limit for RoI detection, substantially improving on the P_d compared to the RoI algorithm. It should be noted that PCS could exceed the statistical limit of RoI, especially for the case of ^{133}Ba (see results in Fig. 4), because the PCS algorithm makes use of features across the entire spectra, meaning that it works with more information than RoI, which is limited to the photopeak region listed in Table I.

Figure 4 and Tables II & III show the MDA_{95} results for both injection isotopes and FAR values as a function of detector number. In the case of $1/7\,\mathrm{hr}^{-1}$ FAR, RoI thresholds are set based on two spectra in the training set, resulting in high variance in the threshold level. As a result, some $1/7\,\mathrm{hr}^{-1}$ FAR RoI scenarios have higher MDA values than would be expected from the broader trend.

As one would expect, the PCS algorithm, using information from the entire spectrum, delivers better performance than RoI across all scenarios. The relative performance gains of PCS for

TABLE II
MINIMUM DETECTABLE ACTIVITY OF ^{137}CS WITH 95% PROBABILITY OF DETECTION (MDA_{95}) (μCI $\pm$*stat.* $\pm$ *sys.*)

		$1/2\,hr^{-1}$ *FAR*			$1/7\,hr^{-1}$ *FAR*		
Det. Type	*Number*	*PCS*	*RoI*	*RoI S.L.*	*PCS*	*RoI*	*RoI S.L.*
HPGe	1	$436^{+29}_{-22} \pm 48$	$530^{+33}_{-24} \pm 59$	$338^{+26}_{-19} \pm 37$	$548^{+35}_{-25} \pm 61$	$530^{+33}_{-24} \pm 59$	$360^{+28}_{-20} \pm 40$
"	3	$210^{+13}_{-10} \pm 23$	$233^{+15}_{-10} \pm 26$	$170^{+13}_{-9} \pm 19$	$226^{+14}_{-10} \pm 25$	$259^{+15}_{-11} \pm 28$	$199^{+14}_{-10} \pm 22$
"	5	$143^{+8}_{-6} \pm 15$	$165^{+10}_{-7} \pm 18$	$126^{+8}_{-7} \pm 14$	$160^{+10}_{-6} \pm 17$	$232^{+12}_{-8} \pm 25$	$148^{+10}_{-8} \pm 16$
"	8	$113^{+6}_{-5} \pm 12$	$137^{+8}_{-5} \pm 15$	$97^{+7}_{-5} \pm 10$	$116^{+7}_{-5} \pm 12$	$156^{+8}_{-6} \pm 17$	$106^{+7}_{-5} \pm 11$
"	11	$94^{+5}_{-4} \pm 10$	$107^{+6}_{-4} \pm 11$	$76^{+5}_{-4} \pm 8$	$99^{+6}_{-4} \pm 11$	$135^{+7}_{-5} \pm 15$	$89^{+6}_{-4} \pm 9$
"	14	$83^{+5}_{-4} \pm 9$	$97^{+5}_{-4} \pm 10$	$68^{+4}_{-4} \pm 7$	$84^{+5}_{-4} \pm 9$	$121^{+5}_{-4} \pm 13$	$77^{+5}_{-3} \pm 8$
NaI	5*	$315^{+17}_{-12} \pm 35$	$430^{+21}_{-16} \pm 48$	$291^{+15}_{-12} \pm 32$	$360^{+17}_{-12} \pm 40$	$457^{+21}_{-16} \pm 51$	$318^{+17}_{-12} \pm 35$
"	10*	$229^{+12}_{-9} \pm 25$	$318^{+15}_{-10} \pm 35$	$202^{+11}_{-8} \pm 22$	$261^{+12}_{-9} \pm 29$	$338^{+15}_{-11} \pm 37$	$221^{+11}_{-8} \pm 24$
"	25*	$134^{+6}_{-5} \pm 14$	$209^{+9}_{-7} \pm 23$	$123^{+7}_{-5} \pm 13$	$144^{+6}_{-5} \pm 16$	$223^{+10}_{-7} \pm 24$	$134^{+6}_{-5} \pm 14$
"	50*	$92^{+5}_{-3} \pm 10$	$131^{+6}_{-4} \pm 14$	$86^{+4}_{-4} \pm 9$	$96^{+5}_{-3} \pm 10$	$144^{+6}_{-5} \pm 16$	$93^{+5}_{-3} \pm 10$
"	75*	$79^{+3}_{-3} \pm 8$	$115^{+5}_{-4} \pm 12$	$70^{+4}_{-3} \pm 7$	$81^{+4}_{-2} \pm 9$	$161^{+5}_{-4} \pm 18$	$76^{+4}_{-3} \pm 8$
"	99*	$67^{+3}_{-2} \pm 7$	$99^{+4}_{-4} \pm 11$	$60^{+3}_{-2} \pm 6$	$78^{+3}_{-3} \pm 8$	$141^{+5}_{-3} \pm 15$	$65^{+3}_{-2} \pm 7$

TABLE III
MINIMUM DETECTABLE ACTIVITY OF ^{133}BA WITH 95% PROBABILITY OF DETECTION (MDA_{95}) (μCI $\pm$*stat.* $\pm$ *sys.*)

		$1/2\,hr^{-1}$ *FAR*			$1/7\,hr^{-1}$ *FAR*		
Det. Type	*Number*	*PCS*	*RoI*	*RoI S.L.*	*PCS*	*RoI*	*RoI S.L.*
HPGe	1	$199^{+12}_{-9} \pm 19$	$282^{+18}_{-12} \pm 28$	$196^{+14}_{-11} \pm 19$	$204^{+12}_{-9} \pm 20$	$297^{+18}_{-13} \pm 29$	$222^{+16}_{-12} \pm 22$
"	3	$91^{+5}_{-4} \pm 9$	$128^{+8}_{-5} \pm 12$	$96^{+7}_{-5} \pm 9$	$92^{+5}_{-4} \pm 9$	$151^{+8}_{-6} \pm 15$	$109^{+8}_{-5} \pm 10$
"	5	$65^{+3}_{-3} \pm 6$	$89^{+5}_{-4} \pm 8$	$72^{+5}_{-3} \pm 7$	$70^{+3}_{-3} \pm 7$	$103^{+6}_{-4} \pm 10$	$84^{+5}_{-4} \pm 8$
"	8	$55^{+4}_{-2} \pm 5$	$74^{+4}_{-3} \pm 7$	$55^{+3}_{-3} \pm 5$	$56^{+3}_{-2} \pm 5$	$86^{+4}_{-3} \pm 8$	$61^{+4}_{-3} \pm 6$
"	11	$45^{+2}_{-2} \pm 4$	$65^{+3}_{-2} \pm 6$	$45^{+3}_{-2} \pm 4$	$45^{+2}_{-2} \pm 4$	$86^{+4}_{-2} \pm 8$	$51^{+3}_{-2} \pm 5$
"	14	$36^{+2}_{-1} \pm 3$	$55^{+3}_{-2} \pm 5$	$39^{+2}_{-2} \pm 3$	$37^{+2}_{-2} \pm 3$	$65^{+3}_{-2} \pm 6$	$43^{+3}_{-2} \pm 4$
NaI	5*	$277^{+15}_{-10} \pm 27$	$507^{+21}_{-15} \pm 50$	$319^{+17}_{-12} \pm 31$	$287^{+15}_{-11} \pm 28$	$555^{+22}_{-16} \pm 55$	$347^{+18}_{-12} \pm 34$
"	10*	$184^{+9}_{-6} \pm 18$	$372^{+16}_{-11} \pm 37$	$221^{+11}_{-8} \pm 22$	$189^{+9}_{-6} \pm 18$	$498^{+17}_{-12} \pm 49$	$240^{+12}_{-8} \pm 24$
"	25*	$126^{+6}_{-4} \pm 12$	$245^{+10}_{-7} \pm 24$	$135^{+7}_{-5} \pm 13$	$129^{+6}_{-5} \pm 12$	$349^{+10}_{-8} \pm 34$	$147^{+7}_{-5} \pm 14$
"	50*	$86^{+4}_{-3} \pm 8$	$179^{+8}_{-5} \pm 17$	$95^{+4}_{-4} \pm 9$	$92^{+4}_{-3} \pm 9$	$200^{+8}_{-5} \pm 20$	$103^{+4}_{-4} \pm 10$
"	75*	$72^{+3}_{-3} \pm 7$	$140^{+5}_{-4} \pm 14$	$78^{+4}_{-3} \pm 7$	$75^{+3}_{-3} \pm 7$	$176^{+6}_{-4} \pm 17$	$84^{+4}_{-3} \pm 8$
"	99*	$67^{+3}_{-3} \pm 6$	$127^{+5}_{-4} \pm 12$	$67^{+3}_{-2} \pm 6$	$70^{+4}_{-2} \pm 7$	$167^{+5}_{-4} \pm 16$	$73^{+3}_{-3} \pm 7$

smaller FAR are, however, of particular note. Figure 4 shows that, in general, for the lower value of FAR (narrow bars) PCS yields larger relative gains in performance compared to RoI, than the higher FAR (wide bars). This result is attributed to improved background estimation by PCS, which has a more pronounced impact for medium-resolution detectors because of the larger overlap of background with spectral features. Additionally, the extent of the performance gain in the HPGe arrays is somewhat surprising, as the specificity of high-resolution systems may be thought to effectively mitigate background clutter, however these findings demonstrate that even high-resolution systems can benefit from analysis with advanced algorithms.

These results were then used to explore how PCS affects performance with respect to the surface area of a detector array (a more intuitive metric than volume for the compactness of an array) and cost of a detector array in question. The cost and surface area of detector arrays is calculated assuming values of \$5k, 100 cm^2 (\$75k, 60 cm^2) per NaI (HPGe) detector. While there are costs associated with the development of an advanced algorithm, they are not included in the comparison. These calculations of cost and surface area enable approximate comparison of array sensitivity (MDA) as a function of value for different sources and false alarm rates. The set of Figures 5, 6 illustrate performance, MDA_{95}, against surface area and cost for both NaI and HPGe arrays of differing sizes when analyzed with different algorithms. Area and cost values for NaI arrays in these figures are calculated based on the estimated 'equivalent' number of unmasked NaI detectors as discussed in Appendix A.

Using the estimates for 'equivalent' unmasked NaI detectors, we find that for detection of the 662 keV γ-ray from ^{137}Cs, which lies above the intense low-energy background feature, the resolution of NaI detectors, regardless of analysis algorithm, is sufficient to yield significantly more sensitivity per unit cost than HPGe arrays, for the range of detector volumes considered here (Fig. 5).

The characteristic γ-rays of ^{133}Ba, on the other hand, lie

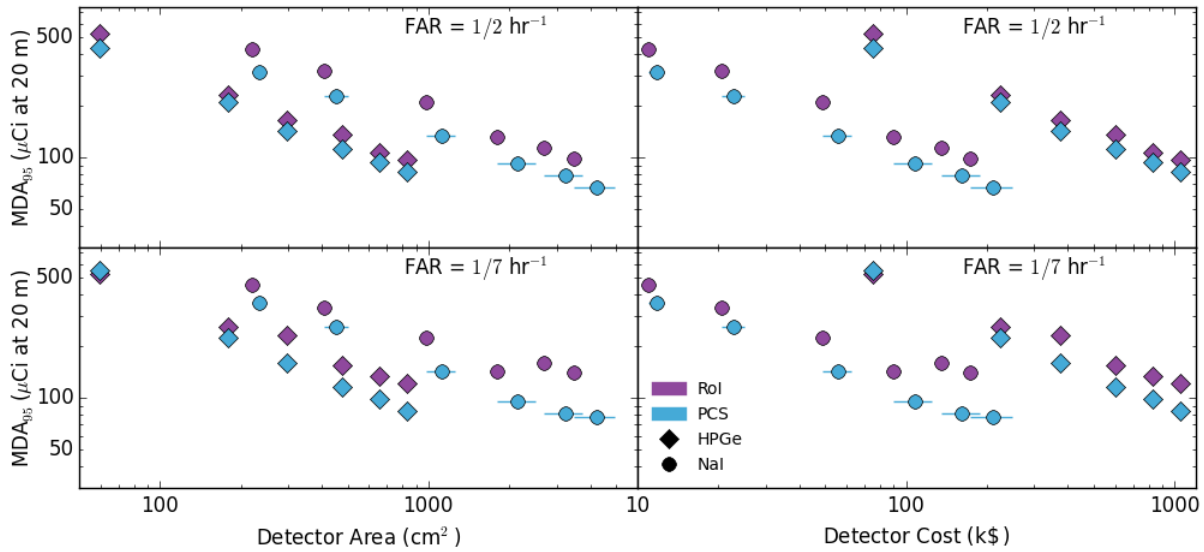

Fig. 5. (Color online) 95% MDA as a function of detector area (left) or cost (right) for detection of a ^{137}Cs at 20 m. Results are shown for a FAR of $1/2\,\mathrm{hr}^{-1}$ in the upper plots and $1/7\,\mathrm{hr}^{-1}$ in the lower plots. Statistical uncertainties are smaller than the data markers. Area and cost values for NaI arrays are calculated based on the estimated 'equivalent' number of unmasked NaI detectors as discussed in Appendix A.

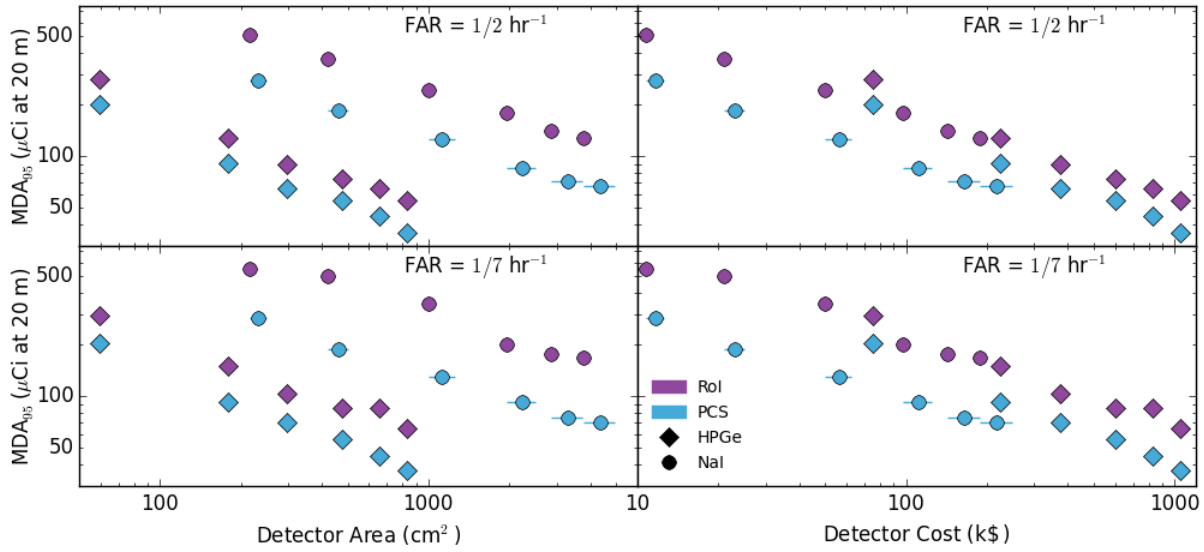

Fig. 6. (Color online) 95% MDA as a function of detector area (left) or cost (right) for detection of a ^{133}Ba at 20 m. Results are shown for a FAR of $1/2\,\mathrm{hr}^{-1}$ in the upper plots and $1/7\,\mathrm{hr}^{-1}$ in the lower plots. Statistical uncertainties are smaller than the data markers. Area and cost values for NaI arrays are calculated based on the estimated 'equivalent' number of unmasked NaI detectors as discussed in Appendix A.

within the intense low-energy background feature. In this case, high-resolution systems yield substantial benefit in detection of the lower energy characteristic γ-rays, and as a result HPGe becomes competitive with NaI in terms of sensitivity per unit cost. While one would expect RoI to yield the highest sensitivity when focusing on only the highest branching ratio photo-peak energy window, PCS is able to effectively utilize information from all photo-peaks and the remainder of the spectrum. As a result, the application of the PCS algorithm yields larger relative performance gains for the medium-resolution system than the high-resolution system for detection of these low-energy γ-rays and can enable NaI arrays to deliver greater sensitivity per unit cost than HPGe (Fig. 6).

This analysis suggests that, given the performance gains afforded by the use of an advanced algorithm such as PCS, algorithm choice should be considered an important factor in the design of a mobile detector array. In many cases, algorithm choice may even be a determining factor in detector system, particularly in scenarios where one expects to encounter complex variations in the natural radiological background.

Consider, for example, the case of a system with a detection sensitivity requirement defined by an MDA_{95} of 100 μCi for the detection of ^{137}Cs from 20 m with a FAR of $1/2\,\mathrm{hr}^{-1}$. Using Fig. 5 as a guide, several of the potential design options can be explored. Examining the performance trends, one may conclude that with only simple detection algorithms at the disposal of the system, the most cost effective solution is represented by a NaI system at a cost close to \$175k and with an area of 3500 cm^2. The most compact solution is represented by a HPGe array with an area of around 720 cm^2 (approximately twelve 100% relative efficiency detectors) but with an associated cost of \$900k.

However, with the introduction of an advanced detection algorithm such as PCS, the detection requirement may be met using a more compact and/or less expensive solution. The most cost effective array would now be represented by an approximately 2000 cm^2 array of NaI detectors at a cost of around \$100k. This represents a factor 1.75 reduction in both surface area and cost relative to the previous system definition. The most compact solution would now be represented by an array of HPGe detectors with a surface area of 600 cm^2 and a cost of \$750k.

One may also contemplate a further example illustrating a common problem where stringent requirements exist for both detection sensitivity and system size. Consider the case where a system with a maximum area of 500 cm^2 must be capable of detecting a 200 uCi source of ^{133}Ba from 20m, with a P_d of 95% and a FAR of $1/7\,\mathrm{hr}^{-1}$. The lower panels of Fig. 6 would suggest that, were a simple detection algorithm to be employed, such a system would necessitate the use of high resolution detectors such as HPGe because an NaI based system would not be capable of meeting the detection sensitivity requirement within the size constraint. The most cost effective HPGe solution would comprise a 180 cm^2 system and come at a cost of around \$225k.

Re-examining the system design while accounting for the performance gains afforded by an algorithm like PCS results in a significantly different conclusion. While applying the advanced algorithm to the HPGe system would result in increased detection sensitivity, the more striking observation is that a NaI-based system would become a viable option, allowing the detection requirement to be satisfied with a 500 cm^2 array. Such a system would cost around \$25k, an order of magnitude less than the HPGe system.

Clearly, the choice of algorithm not only affects the detection sensitivity of a system but may also significantly influence its size and cost, factors which often place fundamental constraints on array design.

IV. Conclusion

The problem of detecting weak γ-sources in complex environments is a challenging one and future solutions will be constrained in several dimensions. To better understand the trade-offs in sensitivity between detector resolution, array size, and analysis algorithm a data set collected by RadMAP was used. RadMAP provides a unique tool for simultaneous collection of γ-ray data with large high and medium-resolution arrays.

TABLE IV
Values of S_ν/B_ν, f, and $f\nu$ at threshold for different NaI array sizes for RoI algorithms

	^{137}Cs			^{133}Ba		
ν^*	S_ν/B_ν	f	$f\nu$	S_ν/B_ν	f	$f\nu$
5*	3.6	0.43	2.2	2.3	0.43	2.15
10*	2.8	0.41	4.1	1.7	0.42	4.2
25*	1.8	0.39	9.8	1.1	0.40	10
50*	1.1	0.36	18	0.8	0.39	19.5
75*	1.0	0.36	27	0.6	0.38	28.5
99*	0.9	0.35	34.7	0.6	0.38	37.6

This data set spanned a variety of urban, suburban, and rural environments, capturing the variability of γ-ray backgrounds. Detection sensitivity was studied for two isotopes, ^{137}Cs and ^{133}Ba, using full spectrum source injection for the specific scenario of passing a source at 15 mph at a closest approach distance of 20 m.

The findings presented here show that the PCS spectroscopic detection algorithm performs better than RoI for both medium- and high-resolution detector arrays and the relative performance gains from PCS improve at lower false alarm rates. Finally, it is shown that the performance gains from PCS, especially with medium-resolution detector arrays, are large enough to significantly impact the design choices for future arrays. As a result, we conclude that the application of advanced algorithms should be considered along with detector array size and resolution when attempting to optimize design within deployment constraints, and the analysis presented here may aide in that process.

Acknowledgements

This work was performed under the auspices of the US Department of Energy by Lawrence Berkeley National Laboratory under Contract DE-AC02-05CH11231.

Appendix A
Considerations on the presence of the passive coded mask

The presence of the passive coded mask in front of the NaI detector array complicates the study of spectroscopic detection, however acquisition with the mask in place is the default configuration of RadMAP. Therefore, to utilize the large amount of data collected by RadMAP, we accept its presence and consider the implications on the findings of this study. First, consider the signal to noise ratio, SNR, of an RoI type algorithm in the Poisson limit at the detection threshold. In this case, for an unmasked array of ν detectors with source and background event rates at threshold of S_ν and B_ν, respectively, $\mathrm{SNR}(\nu) = S_\nu/\sqrt{B_\nu + S_\nu}$. If the array is smaller by a fraction f, we have $\mathrm{SNR}(f\nu) = fS_\nu/\sqrt{fB_\nu + fS_\nu}$. In the case of a masked array the signal to noise ratio is $\mathrm{SNR}(\nu^*) = S^*_\nu/\sqrt{B^*_\nu + S^*_\nu} = MS_\nu/\sqrt{CB_\nu + MS_\nu}$, where M is the ratio of photopeak efficiency of ν detectors without and with the mask ($M = 0.5$ in this study) and C is the ratio of background rate in the RoI without and with the mask.

The ratio of rates with and without the mask, as a function of energy, on RadMAP is shown in Figure 5.1 in [13] for one specific location. From this $C \simeq 0.9$ in the case of ^{137}Cs, and $C \simeq 0.75$ in the case of ^{133}Ba.

This information may then be used to estimate the size of an unmasked array, $f\nu$, with equivalent signal to noise ratio of a masked array of size ν^* at threshold. Setting $\text{SNR}(f\nu) = \text{SNR}(\nu^*)$ and solving yields

$$f\nu = \nu^* \frac{M^2(1 + S_\nu/B_\nu)}{C + MS_\nu/B_\nu}. \quad (4)$$

The mean value of the ratio of $S_\nu/B_\nu = CS^*_\nu/(MB^*_\nu)$, at threshold ($\text{MDA}_{95}$ is used here) is calculated from the injection datasets and is listed in Table IV along with the resultant estimate for the 'equivalent' number of unmasked NaI detectors, $f\nu$. These calculated values of 'equivalent' number of unmasked NaI detectors in the context of RoI algorithms are estimates, and are made to allow some comparison of the performance of unmasked NaI arrays to HPGe arrays. They should be taken in the context of this discussion and a value of $f = 0.5$ should be assumed if a conservative view of the RoI results is desired.

Interpretation of the PCS results for the masked NaI array require a more qualitative discussion. On one hand, collecting data with the mask in place results in more background, than a half-sized unmasked array, due to both down scatter and unmasked directions, thereby making the detection of signal more challenging than in the $f = 0.5$ case. On the other hand, source photons that are down-scattered in the mask may still contribute to an increased PCS response, yielding more source signal than in the $f = 0.5$ case, however this down-scattered signal is still in the Compton continuum of natural background and therefore in a low signal to noise regime. We therefore conclude that the value of f should be smaller than 0.5 in the case of PCS, but not with the same reduction factor as for RoI. We therefore interpret the PCS results for the masked NaI array, in Figs. 5 & 6., with a value of f equidistant between the value computed for RoI and 0.5. Additionally we place a horizontal error bar for these points across this range to further emphasize the uncertainty associated with this qualitative argument. We encourage the reader to recognize the qualitative nature of this argument, and assume a value of $f = 0.5$ for a conservative interpretation of these figures.

REFERENCES

[1] R. C. Runkle, L. E. Smith, and A. J. Peurrung, "The photon haystack and emerging radiation detection technology," *Journal of Applied Physics*, vol. 106, no. 4, 2009.

[2] K.-P. Ziock and K. E. Nelson, "Maximum detector sizes required for orphan source detection," *Nuclear Instruments and Methods in Physics Research Section A: Accelerators, Spectrometers, Detectors and Associated Equipment*, vol. 579, no. 1, pp. 357 – 362, 2007, proceedings of the 11th Symposium on Radiation Measurements and Applications.

[3] K. Ziock, J. Collins, L. Fabris, S. Gallagher, B. Horn, R. Lanza, and N. Madden, "Source-search sensitivity of a large-area, coded-aperture, gamma-ray imager," *Nuclear Science, IEEE Transactions on*, vol. 53, no. 3, pp. 1614–1621, June 2006.

[4] T. Aucott, M. Bandstra, V. Negut, J. Curtis, D. Chivers, and K. Vetter, "Effects of background on gamma-ray detection for mobile spectroscopy and imaging systems," *Nuclear Science, IEEE Transactions on*, vol. 61, no. 2, pp. 985–991, April 2014.

[5] R. Detwiler, D. Pfund, M. Myjak, J. Kulisek, and C. Seifert, "Spectral anomaly methods for aerial detection using {KUT} nuisance rejection," *Nuclear Instruments and Methods in Physics Research Section A: Accelerators, Spectrometers, Detectors and Associated Equipment*, vol. 784, pp. 339 – 345, 2015, symposium on Radiation Measurements and Applications 2014 (SORMA XV). [Online]. Available: http://www.sciencedirect.com/science/article/pii/S0168900215000716

[6] R. C. Runkle, M. F. Tardiff, K. K. Anderson, D. K. Carlson, and L. E. Smith, "Analysis of spectroscopic radiation portal monitor data using principal components analysis," *Nuclear Science, IEEE Transactions on*, vol. 53, no. 3, pp. 1418–1423, 2006.

[7] S. E. Labov, L. Pleasance, P. Sokkappa, W. Craig, G. Chapline, M. Frank, J. Gronberg, J. G. Jernigan, S. Johnson, J. Kammeraad, and et al., *Foundations for Improvements to Passive Detection Systems - Final Report*, Oct 2004. [Online]. Available: http://www.osti.gov/scitech/servlets/purl/15011571

[8] E. LaVigne, G. Sjoden, J. Baciak, Jr., and R. Detwiler, "Extraordinary improvement in scintillation detectors via post-processing with asedra: solution to a 50-year-old problem," vol. 6954, 2008, pp. 695 416–695 416–11. [Online]. Available: http://dx.doi.org/10.1117/12.777295

[9] R. J. Estep, C. W. McCluskey, and B. A. Sapp, "The multiple isotope material basis set (mimbs) method for isotope identification with low-and medium-resolution gamma-ray detectors," *Journal of Radioanalytical and Nuclear Chemistry*, vol. 276, no. 3, pp. 737–741, 2008. [Online]. Available: http://dx.doi.org/10.1007/s10967-008-0626-6

[10] P. Olmos, J. Diaz, J. Perez, G. Garcia-Belmonte, P. Gomez, and V. Rodellar, "Application of neural network techniques in gamma spectroscopy," *Nuclear Instruments and Methods in Physics Research Section A: Accelerators, Spectrometers, Detectors and Associated Equipment*, vol. 312, no. 1, pp. 167 – 173, 1992. [Online]. Available: http://www.sciencedirect.com/science/article/pii/016890029290148W

[11] T. Burr and M. Hamada, "Radio-isotope identification algorithms for nai spectra," *Algorithms*, vol. 2, no. 1, p. 339, 2009. [Online]. Available: http://www.mdpi.com/1999-4893/2/1/339

[12] B. R. Cosofret, K. Shokhirev, P. Mulhall, D. Payne, and B. Harris, "Utilization of advanced clutter suppression algorithms for improved standoff detection and identification of radionuclide threats," *Proc. SPIE*, vol. 9073, pp. 907 316–907 316–13, 2014. [Online]. Available: http://dx.doi.org/10.1117/12.2049831

[13] T. J. Aucott, "Gamma-ray background variability in mobile detectors," Ph.D. dissertation, University of California, Berkeley, 2014.

[14] L. Mitchell, B. Phlips, W. Johnson, E. Wulf, A. Hutcheson, C. Lister, K. Bynum, B. Leas, and G. Guadagno, "Mobile imaging and spectroscopic threat identification (misti): System overview," in *Nuclear Science Symposium Conference Record (NSS/MIC), 2009 IEEE*, Oct 2009, pp. 110–118.

[15] E. I. Novikova, M. S. Strickman, C. Gwon, B. F. Phlips, E. A. Wulf, C. Fitzgerald, L. Waters, and R. Johns, "Designing sword–software for optimization of radiation detectors," in *Nuclear Science Symposium Conference Record, 2006. IEEE*, vol. 1, Oct 2006, pp. 607–612.

[16] J. Curtis, "Benchmarking the Gamma-Ray Response of the Radiological Multi-Sensor Analysis Platform," Master's thesis, University of California, Berkeley, Fall 2014.

[17] L. D. Brown, T. T. Cai, and A. DasGupta, "Interval estimation for a binomial proportion," *Statist. Sci.*, vol. 16, no. 2, pp. 101–133, 05 2001.